Fluid Structure Interaction in aortic dissections

Valerie Deplano, Carine Guivier-Curien

▶ **To cite this version:**

Valerie Deplano, Carine Guivier-Curien. Fluid Structure Interaction in aortic dissections. T. Christian Gasser, Stéphane Avril, John A. Elefteriades. Biomechanics of the Aorta: Modelling for Patient Care, Elsevier Science, In press, Biomechanics of Living Organs series, ISBN-13: 9780323954846. ⟨hal-04232191⟩

HAL Id: hal-04232191

https://hal.science/hal-04232191v1

Submitted on 7 Oct 2023

HAL is a multi-disciplinary open access archive for the deposit and dissemination of scientific research documents, whether they are published or not. The documents may come from teaching and research institutions in France or abroad, or from public or private research centers.

L'archive ouverte pluridisciplinaire **HAL**, est destinée au dépôt et à la diffusion de documents scientifiques de niveau recherche, publiés ou non, émanant des établissements d'enseignement et de recherche français ou étrangers, des laboratoires publics ou privés.

HAL Authorization

Chapter 25

Fluid Structure Interaction in aortic dissections

Valérie. Deplano[1], Carine Guivier-Curien[1]

[1]Aix-Marseille Université, CNRS, Ecole centrale Marseille, IRPHE UMR7342, Marseille, France

Abstract : Aortic dissections (AD) result in two lumens of circulation separated by the neointimal membrane (NIF). Type A ADs requires replacement of the pathological segment but can still evolve in a residual dissection. There are currently no clinical criteria that are sufficiently discriminating to predict this evolution to optimize the patient management. The clinical relevance of numerical modeling to tackle these issues is obvious. However, the choice of the parameters of the elasto-hemodynamic models is decisive. Models including fluid-structure interaction (FSI) are developed. The results highlight that (i) rigid structure modeling overestimates velocities and high wall shear stresses (WSS) values, underestimates low WSS values compared to FSI modeling (ii) a deformable NIF with rigid aortic wall does not bring any significant difference on the flow behavior compared to full rigid modeling (iii) the relevance of FSI analysis is linked to the mechanical behavior of the NIF and dissected descending aorta.

Key Words: Aortic dissection, FSI modeling, Fluid and Structural dynamics, Hemodynamical markers

Abbreviations

AD	Aortic Dissection
BCA	BracioCephalic Artery
CTA	Computed Tomography Angiography
E	Young modulus
ET	Entry Tear
RET	Re Entry Tear
FL	False Lumen
FSI	Fluid Structure Interaction
LCC	Left Common Carotid artery
LS	Left Subclavian artery
TL	True Lumen
NIF	Neo Intimal Flap
RAD	Residual Aortic Dissection
RSV	Ring-shaped vortices
TAAD	Type A Aortic Dissection
TBAD	Type B Aortic Dissection
WSS	Wall Shear Stress
TAWSS	Time Average Wall Shear Stress
Vmax	Maximum velocity
Vmean	Mean velocity

pre proof - author version

1 Introduction

An aortic dissection (AD) occurs when an intimo-medial tear, or entry tear (ET), allows blood flow to enter the aortic wall, thereby creating a patent secondary channel -the false lumen (FL)- which most often propagates distally. True and false lumens are separated by the dissected wall, called the neointimal flap (NIF). According to the Stanford classification, an AD can be either of type A (TAAD) -which involves the ascending aorta- or of type B (TBAD) -which only affects the descending thoracic aorta and below. TAAD is a surgical emergency requiring replacement of the ascending aorta with a prosthesis. Residual aortic dissection (RAD) may persist in the descending segment. It is managed, like other uncomplicated TBAD, by drug treatment. However, in more than 45% of cases (Gaudry et al., 2021) RAD can evolve unfavorably: aneurysmal evolution, ischemia, malperfusion syndrome, aortic rupture requiring a new intervention. The therapeutic management of these lesions is based on preventing the risk of thoracic aorta rupture, which is associated with a very high mortality rate. The risk level is often correlated to some aortic remodeling state which can be defined as changes in the anatomy and function of the aorta. Aortic remodeling can be negative with an unfavorable evolution after an event such as the occurrence of a penetrating aortic ulcer, an intramural hematoma or an aortic dissection, the development of an aneurysm, or positive with stabilized/favorable evolution after treatment. The diameter and number of the ET or re-entry tear (RET), the permeability of the FL, the aortic diameter measurements are all aortic remodeling parameters of RAD (Kimura et al., 2008, Tsai et al., 2014, Zierer et al., 2007) which are used clinically to evaluate the evolutionary risk. However, these clinical indicators are not discriminating enough to predict at early stage the occurrence of a risky evolution of the pathology (Kim et al., 2015, Kimura et al., 2015).

The clinical relevance of *in silico* models to study blood flows and their interactions with biological structures in aortic segments has increased over the past 10 years. In addition to the possibility of performing low-cost parametric studies, the advantage of these models lies in their access to velocity pressure and strain fields at any point and at any time of the cardiac cycle with a spatio-temporal resolution whose only limitation is the associated computation time. This precise mapping of blood flows thus allows an exact spatio-temporal quantification of all the physical quantities associated with their gradients, such as wall shear stress (WSS), time average wall shear stress (TAWSS) or vortical structures, for example, which are known to be a potential marker of the evolution of vascular pathologies (Deplano and Guivier-Curien, 2022). Some of these numerical simulations have so proposed to link the behavior of blood flow in aortic segments to the unfavorable evolution of vascular pathologies through elasto-hemodynamic indexes. However, the relevance of the proposed analyzes depends on the different modeling choices, morpho-mechanical and physical models implemented and boundary conditions. In addition, longitudinal study is needed to associate pathology evolution to biomechanical markers.

AD have not been the subject of much modeling, either numerical or experimental comparing to other vascular pathologies like aneurysms for example. Very rare *in vitro* works investigated artificial compliant AD phantoms and pulsatile flow. In Bjiniuk et al., (2017) or Morris et al., (2022), fluid behavior, flow features were simplified, and flow patterns quantification was not 3D. Zimmermann et al., (2021) used IRM4D to determine velocity fields so that spatial resolution was not sufficient to determine classical velocity gradients biomechanical index. However, it is important to note that none of these *in vitro* works modelized RAD. Among the few works on RAD *in silico* modeling most of them uses rigid wall (Zhu et al., 2021, Khannous et al., 2022) or rigid NIF assumptions (Bonfanti et al., 2017). Few *in silico* works investigated AD through FSI, like Alimohammadi et al., (2015) or Qiao et al., (2019). Moreover, to our knowledge only two studies out of our group (Baumler et al., 2020 and Zhu et al., 2022) performed FSI numerical simulations of RAD. Both studies investigated flow and structures behaviors and the relevance of implementing FSI models. Baumler et al., (2020) did not modelized the prosthesis and focused their work on parametric study related to NIF Young modulus (E_{NIF}) maintaining aortic wall Young modulus (E_{wall}) constant. Their E_{wall} value (800kPa) was lower

pre proof - author version

than this currently used in literature. Qiao et al., (2019) set E_{wall} to 2.7MPa and the lower E_{wall} used by Zhu et al., (2022) was 1.08MPa. They found that E_{NIF} value must be very low (50 to 20kPa) to locally approximate 4DMRI NIF displacements in some locations. They did not compare rigid assumption to FSI one. As Baumler et al., (2020), Zhu et al., (2022) modeled Newtonian fluid. They considered parabolic shape for velocity profile and the same elastic mechanical behavior for aortic wall and NIF. None of them has associated biomechanical markers with adverse evolution through longitudinal follow up.

Using shear thinning fluid behavior the present work proposes to analyze different assumption for structural domain to highlight which structure plays or not a major role in the FSI coupling. In configuration 1 -Rigid-: prosthesis, arterial wall and NIF are all rigid and the numerical simulations consider only the fluid dynamics; in configuration 2 -NIF FSI-: prosthesis and arterial wall are rigid and NIF is compliant – the numerical simulations consider two-way FSI between the fluid and NIF; and finally in configuration 3 -Full FSI-: all the structures have got a Young modulus values and the numerical simulations consider two way FSI between fluid and those structures. On the contrary to our preliminary work considering FSI (Khannous et al., 2020) mechanical behavior of NIF and arterial wall are the same to compare with Zhu et al., 2022. In addition, to discuss the influence of NIF mechanical behavior, NIF FSI investigates two different values for E_{NIF}. Moreover, some biomechanical markers will be linked with adverse evolution through longitudinal follow up.

2 Material and methods

2.1 Geometry

A man – 68 year old – suffering from a TAAD was managed for a surgical procedure during which a Dacron prosthesis was implanted on the ascending aorta. A RAD was still present and treated with drugs. Computed tomography angiography (CTA) was performed at Timone Hospital, Marseille. The CTA images were grouped in a set of 2D 1mm thickness slices with a size of 512x512 pixels and a plane resolution lower than of 0.89mm/px, encoded in 16-bit greyscale. The inter-slice distance was about 1mm. From imaging data, Invesalius 3.1 software (CTI, Brazil) was used to segment and reconstruct the patient's geometry (Figure 1a, d and e). It involved the whole thoracic aorta from above the aorta root to the celiac trunk level, included the 3 aortic arch branches (braciocephalic artery (BCA), left common carotid artery (LCC), left subclavian artery (LS). The ascending segment of the aorta was modeled as a cylinder of D=40mm diameter since it was covered by a prosthesis. The NIF divided the descending aorta lumen in a FL and TL. A main ET and 2 other re-entry tears (RET_1, RET_2) of equivalent sizes (391mm², 424mm², 396mm² for ET, RET_1 and RET_2 respectively) were observed all along the NIF allowing lumens to communicate (Figure 1a). In agreement with the clinician elliptical shapes were chosen to reflect their contours.

The image contrast was not sufficient to correctly obtain the thickness of the aortic wall. Therefore, according to Tang et al., (2005), the aortic wall thickness was assumed to be constant with a value of 2.5mm. With a mean value of 1.85mm, NIF thickness was variable all along the dissection and corresponds to the gap between the TL and FL segmentation. Prosthesis thickness was assumed to get the same value as aortic wall.

The model was thus composed of a fluid domain and a solid domain including NIF, aortic wall and prosthesis.

2.2 Numerical simulations

Ansys Workbench R2 2020 (ANSYS Inc, Canonsburg, USA) was used to perform all the simulations. It includes the fluid solver: Fluent (finite volume method); the solid solver: Mechanical; and the coupling modulus: System Coupling.

pre proof - author version

2.2.1 Fluid domain

The equations to solve were the continuity and the momentum equations

$$\nabla.\overrightarrow{v_f} = 0, \text{ with } \overrightarrow{v_f} \text{ the fluid velocity}$$

$$\rho_f \frac{\partial \overrightarrow{v_f}}{\partial t} + \rho_f((\overrightarrow{v_f} - \overrightarrow{w}).\nabla)\overrightarrow{v_f} = -\nabla p + \nabla.\tau_f$$

with p the fluid pressure, ρ_f = 1060 $kg.m^{-3}$ is the fluid density, τ_f the viscous stress tensor. $\overrightarrow{w}$ is the moving boundary velocity vector (= $\overrightarrow{0}$ when Rigid is considered)

The fluid domain was discretized in 1,276,255 elements (Figure 1b) combining prismatic elements in boundary layers and tetrahedral ones in the core region. 6 elements were set in all around the near wall region to correctly catch the boundary layer δ which thickness was found to be 0.725mm according to Fung's definition. δ=R/α with R the radius and α the Womersley number. Tests were performed to ensure the independence of the solution from the mesh. The maximum cell volume was 2.2mm^3 and the maximum face area was 3.7mm². Since fluid structure interaction was considered, nodes could move, in response to boundary displacements, using a diffusion based smoothing method.

Concerning the numerical schemes, the pressure–velocity linkage was resolved by adopting the iterative solution strategy SIMPLE (Semi Implicit Method for Pressure Linked Equations), least Squares Cell based algorithm was used for spatial discretization of gradients. The pressure was solved through a second order scheme as for momentum. Finally, a second-order implicit scheme was used for time formulation.

To enhance convergence, under relaxations factors were tuned as 0.4 for pressure and 0.6 for momentum. Convergence was assumed when the root mean square residual error was less than 0.001, within a maximum of 50 sub-iterations in a time step.

The unsteady and incompressible flow was assumed to be laminar and the fluid behaved as a shear thinning one using the Carreau Yasuda model with Leuprecht et al., (2001) constants.

$$\frac{\mu - \mu_\infty}{\mu_0 - \mu_\infty} = [1 + (\lambda\dot{\gamma})^a]^{(n-1)/a}$$

with μ_∞=0.0035 Pa.s, μ_0=0.16 Pa.s, λ=8.2s, n=0.2128 and a=0.64

Figure 1b summarizes the fluid boundary conditions. At the entrance, inlet velocity profiles were imposed. They were derived from an ascending aorta flow rate curve from the literature (Olufsen et al., 2000) and defined as the analytical Womersley solution of a fully developed periodic flow in a cylindrical tube. This resulted in a mean Reynolds ($Re_{mean} = \frac{\rho_f v_{fmean} D}{\mu_\infty}$) value of 1279. A maximum Reynolds value of 4785 was found when considering the maximum velocity at ET and the major axis of the ellipsoidal tear shape. Since the minimum critical Reynolds number value (Ab Naim et al., 2014) was 6900 in our case, it justifies the laminar assumption. The Womersley number $\alpha = R\sqrt{\frac{2\pi\rho_f}{T\mu_\infty}}$ (with T the cardiac period =1s) was equal to 27.6.

At the outlets (3 aortic arch outlets BCA, LCC and LS respectively and descending aortic outlet, S), a 3 elements Windkessel model was tuned for each of them, allowing pressure profiles to be defined. For this purpose, optimization algorithm under constraints was performed ensuring that the pressure profile was periodic, and the values were in the range of 80-120mmHg to mimic hypotensive conditions of the patient's treatment. For details see Khannous et al., (2022).

2.2.2 Solid domain

The equation to solve was the momentum equation:

pre proof - author version

$$\nabla . \sigma_s + \overrightarrow{F_s} = \rho_s \frac{\partial^2 \overrightarrow{u_s}}{\partial t^2}$$

where $\overrightarrow{u_s}$ is the solid displacement, σ_s is the solid stress tensor, $\rho_s$the solid density and $\overrightarrow{F_s}$ is the density of forces acting on the solid. Large deformations were allowed, and a Rayleigh damping was turned on with α=50 and β=0.1 to improve the convergence of FSI simulations (Zhu et al., 2022).

The solid domain was discretized in 541,715 tetrahedral elements (Figure 1c). In detail, 72,203 elements for NIF, 436,217 elements for aortic wall and, 33,295 elements for prosthesis. Maximal element length for the aortic wall and prothesis was 2mm and 1.5mm for NIF. Special care has been taken to ensure the conformity of the meshes between the different structural parts.

Both the prothesis and aortic wall were modeled as linear elastic and isotropic materials. The Dacron prosthesis was found to have with a higher Young modulus than the aortic wall one; $E_{prosthesis}$=3.1GPa (Love et al., 2017). Very few data were available in the literature concerning mechanical behavior of TBAD and its NIF. Most of the time TBAD are treated deploying endograft so that *ex vivo* samples are not available. On the contrary TAAD are treated using surgery and some data were published on TAAD and its NIF mechanical behavior. We were thus forced to assume that TBAD had the same behavior than TAAD as found in most of TBAD FSI studies. The Young modulus of the aortic wall derived from echocardiographic measurements (Deplano et al., 2019) on the ascending aorta in which the modulus of Peterson and the morphological parameters (diameter and thickness) have been assessed (Boufi Phd 2016). The value of 1.2MPa was found. This value was in the range of values tested by Zhu et al, (2022).

Figure 1c summarizes the structural boundary conditions that depend on the configurations. For NIF FSI, only NIF was deformable. Element faces facing the aortic wall were embedding $\overrightarrow{u_s} = \vec{0}$. For Full FSI, face prosthesis entrance and main descending outlet were embedding $\overrightarrow{u_s} = \vec{0}$. Normal displacements of aortic branches outlet were not allowed: $\overrightarrow{u_s}.\vec{n} = 0$.

Finally, to model the state of physiological pre-stress, a pressure condition of 80mmHg was imposed on all internal walls of the solid domain. Only resulting constraints were applied to the model to start the simulation with zero displacements.

2.2.3 Fluid-Structure Coupling

Arbitrary Lagrangian Eulerian method was used. Sequentially, fluid and solid equations were solved. Resulting fluid pressures at the interface of domains were transmitted to the solid part which in turn transferred resulting displacements to the fluid part. This 2-way FSI process was performed until convergence. A time step of 0.001s was imposed. Each time step was divided into iteration coupling step.

A maximum root-mean-square residual of 0.01 for both fluid and solid domains and a maximum of 10 iteration coupling steps were imposed to allow convergence of the solution.

The equations to solved at the interface were the kinematic condition $\overrightarrow{v_f} = \frac{\partial \overrightarrow{u_s}}{\partial t}$ and the dynamic condition $\sigma_s.\overrightarrow{n_s} = \sigma_f.\overrightarrow{n_f}$, where subscript f denotes fluid and subscript s denotes solid σ_f is the fluid stress tensor, $\vec{n}$ is the boundary normal vector and $\overrightarrow{n_s} = -\overrightarrow{n_f}$ at the interface

Simulations were performed on Intel® Core i7-8700 CPU machine with 48GB of RAM for C1 and C2 configurations leading to an average computational time for one cycle of about ~ 35h and ~ 72h respectively. For Full FSI modeling, simulations were performed 2 processors Intel® Xeon® CPU E5-2680 machine with 48GB of RAM and took about 170h.

pre proof - author version

To ensure convergence of the solution, several periods were performed. Mean and maximum velocity and pressure values in a longitudinal plane intersecting the entire aorta and in a transversal plane at the RET_1 level were investigated as well as the maximum displacement magnitudes and stresses in the entire aortic wall and NIF. For velocity, in Rigid (NIF FSI and Full FSI respectively) the relative error reached up to 14.5% (15% and 75% respectively) when comparing period 1 versus period 2 whereas it decreases to less than 2.31% (1.66% and 4.9% respectively) when comparing period 2 versus period 3. For pressure, relative error is less than 0.1% when comparing period 2 and 3, whatever the modeling. As far as maximum stresses, respectively displacement magnitudes, were concerned, the relative difference between period 2 and 3 is less than 0.5%, respectively 5.1%, for Full FSI and 0.03% and 0.14% for NIF FSI. In relation to the CPU time, three cardiac cycles were thus considered sufficient to ensure convergence.

3 Results

To test the influence of FSI modeling choices, 3 configurations were investigated: Rigid: all structural parts are assumed rigid, NIF FSI: only NIF is assumed to interact with fluid domain and two different values of E_{NIF} are investigated (1.2MPa (NIF_{12} FSI) and 0.6MPa (NIF_{06} FSI)), Full FSI: all structural parts interact with fluid domain. All the results are examined at the third period.

3.1 Stress and displacement

Von Mises stresses intensity patterns and magnitude of displacements are visible on Figures 2 and 3. When considering Full FSI, a peak of stress, reaching up to 990kPa at t=0.30s, is clearly observed at the junction between prothesis and aortic wall during all along the cardiac period (Figure 2a). It is due to the mismatch of Young modulus between both structures, as already noticed by Zhu et al., (2022) who found equivalent values of 1MPa at their graft-aorta interface. At t=0.30s, high local stress concentrations spots above 180kPa, are found on the inner side of the wall at the departures of the supra-aortic branches and at the junction between aortic wall and NIF (data not shown). At this instant, the mean von Mises stress intensity is 106 kPa on the aortic wall (prosthesis not included) and 57kPa on the NIF. Simultaneously, the maximum of stress recorded in the NIF is found at the ET level on both NIF sides, with a very local peak value at 625kPa. The value of von Mises stresses in the Full FSI are, on average, 100 times higher than those recorded in the NIF_{06} FSI or NIF_{12} FSI model. For NIF_{12} FSI and NIF_{06} FSI, similar patterns of von Mises stresses intensity are observed. When the maximum stress value is compared, a relative difference of 2% is found between both NIF FSI models. The peak intensity is observed sooner than in Full FSI, at t=0.2s, at the ET level, reaching 7.9kPa. Such high intensity values are local in time and space. On average, von Mises stresses are 1.05kPa at t=0.20s. Values remain higher than 3.0kPa around RET_1 during the whole cardiac period whereas stresses are less than 2.0kPa everywhere else.

Displacement values over a period are defined as the displacement magnitude minus the minimum of the displacement magnitude recorded on the period. In Full FSI, the smallest values are found in the prosthesis region because of the highest value of the Young modulus; the more important ones are found in the descending aorta wall with values being about 1.2mm. Such similar observations were done in Zhu et al., (2022) for all their FSI models, where a maximum displacement of 1.34mm was found. The points on ET/RET exhibit the same displacement curves than this of the aortic wall, with a maximum value at t=0.36s, showing that the aortic wall and NIF motion lasts the whole period (Figure 2f). Their displacement follows the pressure curve with a temporal shift of 110ms. We note that, for the NIF, the maximum displacement recorded at RET_1 level is 16%, respectively 12%, higher than this recorded at ET, respectively RET_2. For NIF_{12} FSI and NIF_{06} FSI, the maximum displacement is found at ET level with a peak value of 0.13mm and 0.25mm respectively (Figure 3e). Contrary to what is observed for Full FSI, selected points on each tear do not exhibit the same curves. The displacements peaks are

pre proof - author version

narrower in NIF_{12} or NIF_{06} FSI than in Full FSI reflecting a more rapid NIF motion (Figure 2f versus Figure 3e). Moreover, displacement of all points around RET_1 is quite similar for Full FSI (Figure 2g) whereas it is function of the localization of the considered point for NIF_{06} FSI or NIF_{12} FSI: for right and left point, curves are in opposition showing a shear of the flap (Figure 3f). However, we can observe that from a general point of view, values of displacement are one order of magnitude lower in NIF_{06} FSI or NIF_{12} FSI than in Full FSI modeling.

NIF_{12} or NIF_{06} FSI exhibit very similar behavior as far as structure is concerned and although NIF_{06} FSI displacement values are twice than those observed for NIF_{12} FSI, these low values of less than half a millimeter suggest that the flows will be very similar for these two configurations. From now on, we will only deal with NIF_{12} FSI that will be simplified in NIF FSI.

3.2 General flow features

Khannous et al., (2022) described the flow patterns in two different models of RAD for rigid wall assumptions. They underlined that flow behavior is piloted by the complex morphologies of the geometries, depending on tortuosity, curvature, number, size and location of ET/RET and size of section widening. To describe highly 3D patterns of the flow behavior, streamlines are plotted at different instants of the cardiac cycle for Full FSI modeling (Figure 4). NIF, aortic wall and two perpendicular planes (P_2 and P_4) located between the RET_1 and RET_2 and between RET_2 and the outlet are materialized by transparency to better highlight the fluid dynamics. View is oriented towards the FL. Animations with view orientations towards FL and TL are also available in supplementary material. The particles are released from a plane just upstream of ET and parallel to it. Due to narrowing of the ET/RET and the flow rate acceleration, jet flows are generated through the ET/RET. Narrowed lumen in distal part of the aorta exhibits the same pattern. Zhu et al., (2022) described the same features for narrowing. Visible from t=0.075s for ET and from t=0.125s for all the ET/RET, these jets are directed from TL to FL all along the cardiac cycle. They impact the aortic wall of the FL as early as t=0.125s for ET and around t=0.225s and t=0.175s for RET_1 and RET_2 respectively. When entering in FL, as the flow rate decelerates, they are surrounded by recirculation areas that can be clearly observed for example downstream ET in the section widening. Fluid patterns become increasingly disturbed after the jet impact and zeroing of the flow rate (t=0.35s). The 3D vortical structures (see 3.4) that appear during the acceleration phase exhibit complex dynamics evolutions during diastolic phase.

It is important to underline that for a given RAD morphology, whatever the conditions for the structural domain (Rigid, NIF FSI or Full FSI), the general fluid characteristics and temporal evolution are equivalent. For Full FSI modeling aortic wall expands during systolic phase and retracts during diastolic one; NIF is deformable and can move. For NIF FSI, the aortic wall is rigid, but NIF is deformable and can move. To highlight some quantitative differences between the models, velocity values are recorded in the whole fluid domain. Considering the whole cardiac period, the mean velocity resulting from rigid modeling overestimates by 30.5% and 3.75% on average this from Full FSI and NIF FSI modeling respectively. To investigate the velocity intensities at the ET/RET, a volume of interest is defined. This volume is a sphere centered on the tear area and which radius is defined as 5/6 of the width of the tear measured in a plane intersecting it by it middle. Except for accelerating phase, Rigid and NIF FSI are quantitatively similar with a maximum difference of 5.1% and 2.89% in ET/RET volume for the maximum velocity (Vmax) and mean velocity (Vmean) respectively. At t=0.075s the percentage of difference reaches 8.4% and 12.5% for Vmax and Vmean respectively. Velocities are sometimes overestimated or underestimated. On the contrary, most of the time, Rigid model overestimates Vmax and Vmean in ET/RET volume in comparison to Full FSI. This overestimation is expected since the widths of the ET/RET expand all along the cardiac cycle. This overestimation is more important for RET_2 and during diastolic phase, t=0.375s, it reaches 48.66% and 65% for Vmax and Vmean respectively versus 21.14% and 21.63% at t=0.15s the peak of flow rate. It is interesting to note that the

Pre-proof - author version

velocities in ET volume are higher than in RET_1 or RET_2 ones whatever the modeling. At t=0.15s for Full FSI, Vmax is 17.96% and 26.57% higher in ET than in RET_1 and RET_2 respectively. However, for ET the overestimation is lower with only 2.52% at t=0.15s and 23.23% at t=0.375s considering Vmax. Moreover, during the accelerating phase (t=0.075s) Rigid model underestimates Vmax at ET volume of about 13% in comparison to Full FSI modeling.

3.3 Flow rate repartition

Figure 5 shows the flow rate repartition in each lumen for inter tear planes P1, P2 and P3, allowing to visualize the contribution of each ET/RET in the flow rate repartition and to go further with quantification of the flow feature differences between the models.

Flow rate curve shape and values observed in rigid and NIF FSI modeling are similar with a maximum of 5.2% of difference at the peak systolic phase, whatever the lumen and the plane of interest. Whatever the configuration (Rigid, NIF FSI or Full FSI), in P1, flow rate is higher in TL than in FL, whereas the contrary is observed in P2 and P3: the flow rate in TL decreases in benefit of FL. In P1, respectively P2 and P3, the peak flow rate ratio in FL versus TL is 42%, respectively 134% and 387% in Rigid and 58%, 132% and 345% in Full FSI. RET_1 and RET_2 allow for the continuous supply of FL. Baumler et al. (2020) did not find such differences between TL and FL whatever the model they considered, but only one entry tear was present in their study.

All along the cardiac period in P1, TL flow rate is overestimated by Rigid modeling up to 12% in comparison to Full FSI one with a slight time lag for peak value (Δt=0.025ms), whereas it is underestimated in FL by 18% at the flow rate peak. In P2, rigid modeling overestimates the flow rate values in TL and FL in comparison to Full FSI one (by 21% at the peak for TL and 24% for FL) except at the end of the diastolic phase (from t=0.8 to 1.0s) in FL. One can note that the maximum flow rate in FL is reached sooner than in TL for Full FSI modeling (Δt=75ms) whereas maxima are found to be reached simultaneously in TL and FL for rigid assumption. In P3, rigid modeling overestimates flow rate values in TL, respectively in FL, by 29%, respectively 44%, when the maximum value are compared. However, in TL, from 0.325s to the end of the cardiac cycle, the Rigid underestimates the Full FSI by 26% on average.

3.4 Vortical structure evolution

Jet flow through ET/RET entering in FL showing a section widening, presents a velocity discontinuity at the jet boundaries resulting in a rolling up shear layer. This creates 3D vortical structures that propagate in the FL. They are identified using the λci criterion which is based on the imaginary part of the complex conjugate eigenvalues of the velocity gradient tensor (Zhou et al., 1999). Figure 6 shows the temporal evolution of the λci iso contours for Rigid and Full FSI modeling. According to general fluid features the vortical structure evolutions are similar. Ring-shaped vortices (RSV) form at the necks of the ET during the acceleration phase (t=0.075s). At t=0.15s they all detach from ET/RET necks. Different shapes are then observed, RSV from ET and RET_2 lost their ring shape and flattened along the FL curvature, while RET_1 keeps its ring shape. Vortical structures are then convected downstream and impact the FL external wall around t=0.25s. After their impact, they subdivide into smaller structures and dislocate during the end of the diastolic phase. Some differences appear between the modeling mainly from the pressure peak at t=0.25s instant from which the rigid model overestimates vortical structure in FL. This overestimation is quantified by calculating the surface covered by the λci, which indicates their cumulative importance. For rigid model their surface is greater than 12.02% at t=0.075s, reach 45.23% at t=0.25s and 109.74% at the end of the cardiac cycle. This overestimation is expected since for Full FSI aortic wall and ET/RET widths expand.

pre proof - author version

3.5 WSS and TAWSS distributions

According to the flow features and as described in the literature WSS values are the highest during systolic phase at ET, curvatures, or plications, and at walls where jet flow impacts (Figure 7). At ET/RET locations, values are higher than 25Pa at maximum of flow rate (t=0.15s) whatever the assumption of modeling (see appendix A). Figure 7 shows the comparison between the different structural boundary conditions. Although WSS features are equivalent, Rigid wall and NIF_{12} FSI modeling (Figure 7a and b) overestimate the maximum WSS values at t=0.15s and 0.25s and underestimate during the acceleration phase (t=0.075s) (see appendix A). The overestimation and underestimation can reach 55% and 27% respectively. In Rigid, surface of TAWSS with values higher than 9Pa are 17.89 times larger than those encountered in Full FSI (Figure 7 g-j). However, the maximum TAWSS values at ET and RET_2 are always higher than 10Pa whatever the assumption of modeling (see appendix A).

Regions of low WSS (≤ 0.5 Pa) occur all along the cardiac cycle. For Full FSI modeling they cover 41.6% of the total structure surface at t=0.075s. This percentage increases throughout the cardiac cycle to reach 69% at t=0.375s and 97.4% at the end of the period. Rigid wall assumption underestimates the surfaces of low WSS by 55.48% at t=0.075s, 23.08% at t=0.375s and 1.79% at t=1s. Considering TAWSS, Rigid and NIF FSI modeling underestimate these surfaces of 21.03% and 16.63% respectively. Such underestimation agrees with the literature (Alimohammadi et al., 2015).

3.6 Pressure repartition

Whatever the modeling, mean pressure values are higher in the upper part of the aorta (P1 plane) than in the lower part (P3 plane) up to t=0.225s, after that, the trend reverses (Figure 8a). It is however important to underline that the pressure differences never exceed 1.5mmHg between P1 and P3 planes (ΔP=1.42mmHg and 1.17mmHg for rigid and Full FSI modeling respectively). These results agree with literature (Ab Niam et al., 2016), Alimohammadi et al., 2014). Whatever the model, mean pressure values are higher in the TL than in the FL throughout almost the entire cardiac cycle, for P1, P2 and P3 planes (Figure 8c, d and e) in accordance with the single direction of blood exchange between the two lumens revealed by the flow rate distribution. Once again, the differences of mean pressure between the lumens, ΔP_{TL-FL}, are small and always lower than 1.34mmHg.

Whatever the considered planes (Figure 8b) mean pressure values are overestimated by the Rigid modeling up to t=0.2s and underestimated between 0.2s and 0.4s. Again, the differences never exceed 2.6mmHg and the maximum of overestimation is about 0.03%.

3.7 Hemodynamical markers

WSS values higher than 10Pa activate platelets (Hellums et al., 1987), a stress level of about 18Pa can induce their aggregation and, adhesion of activated aggregated platelets to the arterial wall occurs when WSS/TAWSS values are low (< 0.5 Pa ; Ab Naim et al., 2016). It is now well known that this process initiates thrombus formation. Vortical structures form at the ET/RET necks from the beginning of the cardiac cycle, detach from the necks, are convected downstream to the FL lower segment where they break up near the FL wall downstream RET_2. This dynamic takes place whatever the modeling (see 3.4). In context of rigid modeling, thanks to patient follow up, it has been possible to discriminate favorable and unfavorable evolution of the pathology (Khannous et al., 2022) showing that such 3D vortices dynamics associated to high WSS values at ET/RET and low ones at FL wall play a role in thrombus formation through their action on platelets. Platelets are actually trapped, convected and released by the 3D vortices. Although rigid modeling overestimates the maximum WSS values at t=0.15s and 0.25s, the maximum values at ET and RET_2 always exceed 20Pa for Full FSI modeling. Furthermore, rigid modeling underestimates surfaces of WSS values lower than 0.5Pa. Therefore, thrombus formation in FL, via vortical structure locations and levels of WSS values, is confirmed for Full FSI modeling. Figure 1 shows the clinical evolution of the patient between the initial time of the follow up (Figure 1d) and one year later (Figure 1e). Thrombus does not exist in the lower part of the

pre proof - author version

FL at initial time and can be clearly observed 1 year later on CT-angioscan downstream RET_2 as predicted by modeling.

4 Discussion and conclusion

Residual aortic dissections are more complex to model than other aneurysmal pathologies such as thoracic or abdominal aneurysm for example. The two main reasons are the presence of NIF with entry and re entry tears and the interaction of the fluid with three different structures with their own mechanical behavior. In addition, since RAD and TBAD are usually treated with TEVAR, *ex vivo* samples of dissected descending aortic wall or/and NIF are extremely rare. Moreover, *in vivo* data using MRI to record NIF and descending aorta wall motions are currently confidential. In that context, FSI modeling suffers from an obvious lack of data whereas their exploitation can give insights in the evaluation of the pathology. Considering the huge effort to perform Full FSI modeling of RAD versus rigid one, both on computation time and *in vivo* data collection, it is necessary to get more information on the importance to perform complex modeling such FSI one to answer clinical issues.

Our modeling considers i) patient specific RAD morphology, ii) two-way FSI, ii) shear thinning blood behavior, iii) inlet velocity profile with Womersley shape and from flow rate recorded at ascending aorta inlet, iv) Windkessel models at outlets, v) pre-stressing, vi) prosthesis presence and vii) patient follow up improves the understanding of the influence of aortic wall and NIF motions on fluid and structure dynamics.

Our results underline that considering a deformable NIF with rigid aortic wall does not bring any significant difference on the flow behavior compared to simulations where all structures would be rigid even for low E_{NIF} value. Full FSI modeling exhibits some specific characteristics compared to rigid one. As far as the fluid is concerned velocity values and flow rates in TL and FL are mainly overestimated by rigid model. The overestimation of pressure resulting from rigid model in both lumen is so small that it can be considered negligible. Finally, it is important to highlight that despite these differences, both models can predict thrombus formation at early stage.

On the structure side, Full FSI modeling give information on the levels of displacements of aortic wall and NIF and those of the stress applied on these structures. NIF and aortic wall maximum displacements exhibit the same curve shape with maximum value around 1.2mm for Full FSI modeling whereas for NIF FSI modeling the NIF displacements seems negligible even for the most compliant NIF. These results are in line with flow behavior. Excepted at the connection between the prosthesis and the ascending aorta, the level of highest stress encountered on aortic wall, ~200kPa, is below the threshold of rupture (Duprey et al., 2016). However, such a stress value can participate to the aortic wall expansion as showed by Shang et al. (2013) for a descending thoracic aneurysm. To our knowledge, no work deals with threshold of stress value for ET/RET widening but it could be interesting to investigate the relation between peak stress value at ET/RET and their enlargement.

It is important to note that these results are highly dependent on the mechanical behavior of the different structures namely E_{wall}, E_{NIF} and $E_{prosthesis}$ and more particularly on the difference between E_{wall} and E_{NIF}.

E_{wall} was set to 1.2MPa to be able to compare with Zhu et al. (2022) work. However, this value is found for ascending aorta Young modulus. Moreover, it is now well known that aortic wall Young modulus value depends both of location -ascending or descending- thoracic aorta and of aorta state -healthy or pathological-. According to the literature ascending aorta is more compliant than descending aorta (Boccadifuoco et al., 2018) and pathological segments are stiffer than healthy one (Emmott et al., 2016). In addition, it seems unlikely that E_{NIF} is equal to E_{wall} considering that NIF does not include any adventitia layer. *In vivo* data on NIF displacements of thoracic aorta show unexplained large variations: 0.48-0.68mm for Karmonik et al., (2012), 1.3mm for Ganten et al., (2009), up to 8.7mm in Baumler et al., (2020). The two Full FSI modeling of RAD (Zhu et al., 2022 and Baumler et al., 2020) report the

pre proof - author version

same large variations respectively. Baumler et al., (2020) concluded that the NIF motion substantially influences local hemodynamics. However, to obtain *in silico* NIF displacements in the range of those recorded by MRI (8.7mm) they set E_{NIF} to a very low value: 20kPa. This value is 40 times lower than this used for aortic wall (E_{wall}=800kPa). More broadly, in TBAD modeling, a wide range of values are chosen to model the NIF, from E_{NIF} =1.3 MPa for Zimmermann et al., (2021) to 6.75 MPa for Chong et al., (2020). To our knowledge there is no work on mechanical behavior of NIF from RAD to compare with such a value. However, few works performed tensile tests on NIF from TAAD. Our group (Deplano et al., 2019) found that NIF from TAAD exhibits a quasi linear anisotropic behavior in the range of 20% of deformation. Without considering the anisotropic feature we determined an E_{NIF} value of 0.51MPa. Moreover, in the same study, *in vivo* transoesophageal echocardiography measurements performed on 13 TAAD patients reveal a mean E_{wall} of 5.39MPa e.g only 10 times higher than E_{NIF}. It seems that the understanding of large *in vivo* NIF displacements cannot be only explained by decreasing E_{NIF}. Finally, the relation between NIF motion, whatever its amplitude, and very small pressure difference between FL and TL, ΔP_{TL-FL}, never higher than 5mmHg is not trivial. Dimensions and localization of ET and RET, number of RET and peripherical resistance certainly also play a role in the local NIF motion. This point seems to be an essential key to understand mechanisms implicated in RAD main remodeling characteristics.

Apart from fluid boundary conditions, the flow and structural behavior mainly depend on RAD morphology especially on tear and re entry tears features and on the stiffness of dissected aortic wall and NIF which are intrinsically dependent on each other. Influence of NIF on flow behavior cannot be analyzed only modeling its mechanical behavior, that of the aortic wall must also be taken into account. Obviously, only Full FSI modeling assesses stress intensities used to identify potential vulnerability of some wall regions to widen or rupture. In addition, stresses and stretches assessment associated with flow dynamics can help to find out new elasto-hemodynamical markers to discriminate unfavorable RAD evolution. However, without *in vivo* information on descending aorta NIF mechanical behavior it seems difficult to conclude that Full FSI modeling is essential to tackle clinical problems related to the early prediction of the evolution of RAD.

The main limitation of the present work is indeed related to the lack of *in vivo* data on the mechanical behavior of the NIF and its related dissected descending aorta. The two values cannot be dissociated to study the prediction of descending aortic remodeling. Moreover, to allow structural simulation, a boundary must be fixed, preventing the aorta from a full 3D motion that is clinically observed. In our study, the main outlet is fixed while upstream the aorta is free to expand leading to the appearance artificial peripherical resistance. Nevertheless, thanks to our ongoing work using cine MRI (Baudouard et al., 2022), the whole movement of the aorta over the cardiac period is recorded. New computational fluid dynamics models integrating these movements are being developed while avoiding the issue of the mechanical behavior of the aorta and the sometimes-prohibitive computation time of the FSI.

Finally, flow and structure dynamics were studied in only one patient specific morphology. All the features we described are obviously highly dependent on geometrical and mechanical characteristics of the aorta and of the NIF. To be clinically relevant, a larger cohort of patients must be included. Advances in deep learning physics inspired should help in dealing with a larger number of cases with variability in morphologies and material parameters while avoiding long computational time inherent to fully FSI modeling.

pre proof - author version

Acknowledgments

We acknowledge the Department of Vascular Surgery of the Timone Hospital in Marseille and more particularly Gaudry Marine, PhD, Md.

pre proof - author version

Appendix A

Maximum values of WSS at ET/RET during the systolic phase (0<t<0.3s) for the different modeling

	Time (s)	**Max of WSS at ET (Pa)**	**Max of WSS at RET_1 (Pa)**	**Max of WSS at RET_2 (Pa)**
RIGID	0.075	25.2823	10.1396	18.6390
RIGID	0.150	43.7341	29.4579	52.6440
RIGID	0.250	36.9462	27.9514	54.2117
NIF_{12} FSI	0.075	29.4960	9.4165	16.8372
NIF_{12} FSI	0.150	45.6638	27.6478	52.9992
NIF_{12} FSI	0.250	36.0883	25.6400	55.6125
FULL FSI	0.075	34.7670	12.2998	20.5086
FULL FSI	0.150	43.6679	25.6073	43.5875
FULL FSI	0.250	27.0381	17.9453	35.7040

Percentage of relative difference of maximum values of WSS at ET/RET between the different modeling during the systolic phase

		$(\max(WSS)-\max(WSS_{FULL\ FSI}))/\max(WSS_{FULL\ FSI})$ (%)		
	Time (s)	At ET	At RET_1	At RET_2
RIGID	0.075	-27.28	-17.56	-9.12
RIGID	0.150	0.15	15.04	20.78
RIGID	0.250	36.65	55.76	51.84
NIF_{12} FSI	0.075	-15.16	-23.44	-17.90
NIF_{12} FSI	0.150	4.57	7.97	21.59
NIF_{12} FSI	0.250	33.47	42.88	55.76

Maximum value of TAWSS at ET/RET for different structural domain boundary conditions

	ET	RET_1	RET_2
RIGID	13.801 Pa	9.713 Pa	19.553 Pa
NIF_{12} FSI	13.904 Pa	8.960 Pa	18.291 Pa
FULL FSI	10.641 Pa	6.311 Pa	13.879 Pa

pre-proof author version

References

Ab Naim, W.N., Ganesan, P.B., Sun, Z., Osman, K., Lim, E. (2014) The impact of the number of tears in patient-specific Stanford type B aortic dissecting aneurysm: CFD simulation. J Mech Med Biol 14(2):1450017.

Ab Naim WN, Ganesan PB, Sun Z, Liew YM, Qian Y, Lee C-J, Jansen S, Hashim SA, Lim E (2016) Prediction of thrombus formation using vortical structures presentation in Stanford type b dissection: a preliminary study using CFD approach. Appl Math Model 40:3115–3127.

Alimohammadi M, Agu O, Balabani S, Diaz-Zuccarini V (2014) Development of a patient-specific simulation tool to analyze aortic dissections: assessment of mixed patient-specific flow and pressure boundary conditions. Med Eng Phys 36:275–284.

Alimohammadi, M., Sherwood, J.M., Karimpour, M., Agu, O., Balabani, S., and Díaz-Zuccarini, V. (2015) Aortic dissection simulation models for clinical support: fluid-structure interaction vs. rigid wall models. BioMed Eng OnLine 14, 34.

Baudouard, M., Rapacchi, S., De Masi, M., Guivier-Curien, C., Jacquier, A., Deplano V. 2022. Motion assessment of the thoracic aorta for flow numerical modeling. Compt. Meth. Biomech. Biomed. Eng. (in press).

Bäumler, K., Vedula, V., Sailer, A.M., Seo, J., Chiu, P., Mistelbauer, G., Chan, Michael, F.P., Fischbein, P., Marsden, A.L., Fleischmann, D. (2020) Fluid–structure interaction simulations of patient-specific aortic dissection. Biomechanics and Modeling in Mechanobiology. https://doi.org/10.1007/s10237-020-01294-8

Boccadifuoco, A., Mariotti, A., Capellini, K., Celi, S., Salvetti, M.V. (2018). Validation of Numerical Simulations of Thoracic Aorta Hemodynamics: Comparison with In Vivo Measurements and Stochastic Sensitivity Analysis. Cardiovasc Eng Tech 9: 688–706. https://doi.org/10.1007/s13239-018-00387

Bonfanti, M., Balabani, S., Greenwood, J.P., Puppala, S., Homer-Vanniasinkam, S., Díaz-Zuccarini, V. (2017). Computational tools for clinical support: a multi-scale compliant model for haemodynamic simulations in an aortic dissection based on multi-modal imaging data. J. R. Soc. Interface 14: 20170632.

Boufi, M. Caractérisations morphométriques et biomécaniques de l'aorte thoracique, Phd (2016)

Deplano, V. and Guivier-Curien, C. (2022). Geometric vascular singularities, hemodynamic markers and pathologies (Chapter 3). Edition ISTE-WILEY. Biological flow in large vessels; Dialog between numerical modeling and in vitro/in vivo experiment.

Deplano, V., Boufi, M., Gariboldi, V., Loundo, A.D., D'Journo, X.B., Cautela, J., Djemli, A., Alimi, Y., (2019). Mechanical characterisation of human ascending aorta dissection. Journal of Biomechanics, 94, 138-146.

Duprey, A., Trabelsi, O., Vola, M., Favre, JP., Avril, S. (2016). Biaxial rupture properties of ascending thoracic aortic aneurysms. Acta Biomaterialia, 42 : 273-285

Emmott, A., Garcia, J., Chung, J., Lachapelle K., El-Hamamsy, I., Mongrain, R., Carrier, R., Leask, R.L (2016). Biomechanics of the Ascending Thoracic Aorta: A Clinical Perspective on Engineering Data. Canadian Journal of Cardiology 32 (2016) 35e47

Fung YC (1996) Biomechanics. Circulation. Springer, New York

Gaudry, M., Porto, A., Guivier-Curien C., Blanchard, A., Bal, L., De Masi, M., Ejargue, M., Jacquier, A., Gariboldi, V., Deplano, V., Piquet, P., (2021). Results of a prospective follow-up study after type A aortic dissection repair: a high rate of distal aneurysmal evolution and reinterventions. Eur. J. of Cardio-Thoracic Surg, https:/doi/10.1093/ejcts/ezab317.

Ganten, M-K., Weber, T.F., von Tengg-Kobligk, H., Böckler, D., Stiller, W., Geisbüsch, P., Kauffmann, G.W., Delorme, S., Bock, M., Kauczor, H-U. (2009) Motion characterization of aortic wall and intimal flap by ECG-gated CT in patients with chronic B-dissection. Europ. J Radiol, 72(1): 146-153.

pre proof - author version

Hellums, J.D., Peterson, D.M., Stathopoulos, N.A., Moake, J.L., Giorgio, T.D. (1987) Studies on the mechanisms of shear-induced platelet activation. In: Hartmann A, et Kuschinsky W (eds) Cerebral Ischemia and Hemorheology. Springer, Berlin, pp 80–89

Kim, J.B., Kim, K., Mark, BA; Lindsay, E., MacGillivray, T.; Isselbacher, E.M.; Cambria, R.P., Sundt II, T.M., (2015) Risk of rupture or dissection in descending thoracic aortic aneurysm. Circulation, 27;132(17).

Kimura, N., Itoh, S., Yuri, K., Adachi, K., Matsumoto, H., Yamaguchi, A., Adachi, H. (2015) Reoperation for enlargement of the distal aorta after initial surgery for acute type A aortic dissection. J Thorac Cardiovasc. Surg., 149(2).

Kimura, N., Tanaka, M., Kawahito, K., Yamaguchi, A., Ino, T., Adachi, H., (2008) Influence of patent false lumen on long-term outcome after surgery for acute type A aortic dissection. J Thorac. and Cardiovasc. Surg., 136(5).

Khannous, F., Guivier-Curien C., Gaudry, M., Piquet Ph., Deplano, V. (2022). Numerical modeling of residual type B aortic dissection: longitudinal analysis of favorable and unfavorable evolution. Medical and Biological Engineering and Computing DOI: 10.1007/s11517-021-02480-1

Khannous, F., Guivier-Curien, C., Gaudry, M., Piquet, Ph., Deplano, V. (2020). Residual type B aortic dissection FSI modeling. Computer Methods in Biomechanics and Biomedical Engineering, 23(1), 153-155. doi 10.1080/10255842.2020.1812165.

Leuprecht, A., Perktold, K. (2001) Computer simulation of non-newtonian effects on blood flow in large arteries. Comput Method Biomech Biomed Eng 4:149–163

Love, B. (2017). A systems approach to engineering concepts. Academic Press.

Olufsen, M.S, Peskin, C.S., Kim, W.Y., Pedersen, E.M., Nadim, A., Larsen, J. (2000) Numerical simulation and experimental validation of blood flow in arteries with structured-tree outflow conditions. Ann Biomed Eng 28:1281–1299

Qiao, Y., Zeng, Y., Ding, Y., Fan, J., Luo, K. Zhu, T. (2019) Numerical simulation of two-phase non-Newtonian blood flow with fluid-structure interaction in aortic dissection. Computer methods in biomechanics and biomedical engineering.

Shang, E.K., Nathan, D.P., Sprinkle, S.R., Vigmostad, S.C., Fairman, R.M., Bavaria, J. E., Gorman, R.C., Gorman J.H., Chandran K.B., Jackson B.M (2013) Peak wall stress predicts expansion rate in descending aortic aneurysms. Ann. Thorac. Surg., 95(2): 593-598.

Tsai, M.T., Wu, H.Y., Roan, J.N., Tsai, Y.S., Hsieh, P.C.H., Yang, Y.J., Luo C.Y., (2014) Effect of false lumen partial thrombosis on repaired acute type a aortic dissection, J Thorac Cardiovasc. Surg., 148.

Zhu, Y., Mirsadraee, S., Asimakopoulos, G., Gambaro, A., Rosendahl, U., Pepper, J., Xu, X.Y. (2021). Association of Hemodynamic Factors and Progressive Aortic Dilatation Following Type A Aortic Dissection Surgical Repair. Sci. Rep. 11, 1–13. doi:10.1038/s41598-021-91079-5

Zhu, Y., Mirsadraee, S., Rosendahl, U., Pepper, J. and Xu, XY. (2022) Fluid- Structure Interaction Simulations of Repaired Type A Aortic Dissection: a Comprehensive Comparison With Rigid Wall Models. Front. Physiol. 13:913457. doi: 10.3389/fphys.2022.913457

Zierer, A., Voeller, R.K., Hill, K.E., Kouchoukos, N.T., Damiano Jr, R.J., Moon, M.R. (2007) Aortic enlargement and late reoperation after repair of acute type A aortic dissection. Annals of Thorac. Surg., 84(2).

pre proof – author version

Zimmermann, J., Bäumler, K., Loecher, M., Cork, T.E., Kolawole, F.O., Gifford, K., Marsden, A.L., Fleischmann, D., Ennis, D.B. (2021). Quantitative Hemodynamics in Aortic Dissection: Comparing in vitro MRI with FSI Simulation in a Compliant Model. In: Ennis, D.B., Perotti, L.E., Wang, V.Y. (eds) Functional Imaging and Modeling of the Heart. FIMH 2021. Lecture Notes in Computer Science, vol 12738. Springer, Cham.

pre proof - author version

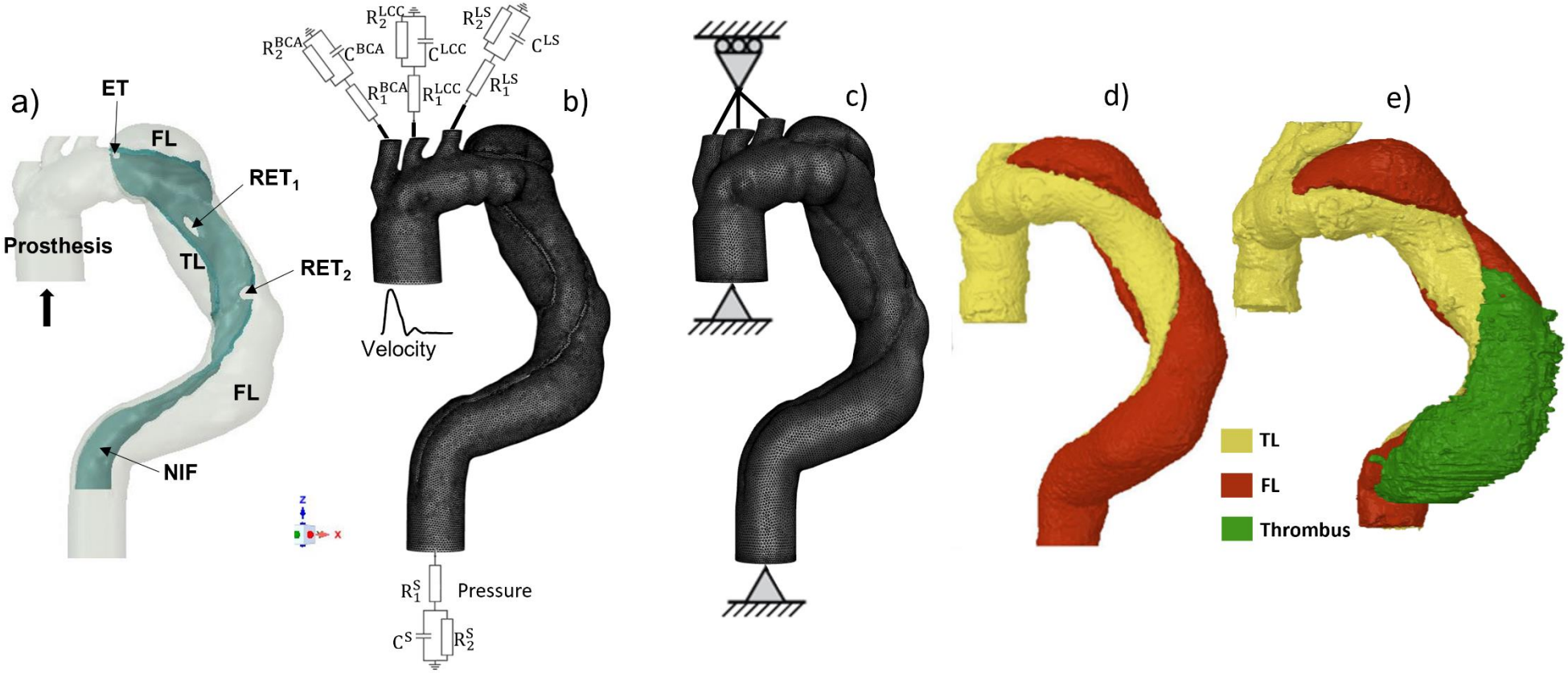

Figure 1 : RAD geometry. b) Mesh and fluid boundary conditions. c) Mesh and structural boundary conditions. d) RAD morphology from CT scan just after the prosthesis implantation. e) RAD morphology from CT scan one year after the prosthesis implantation.

pre proof

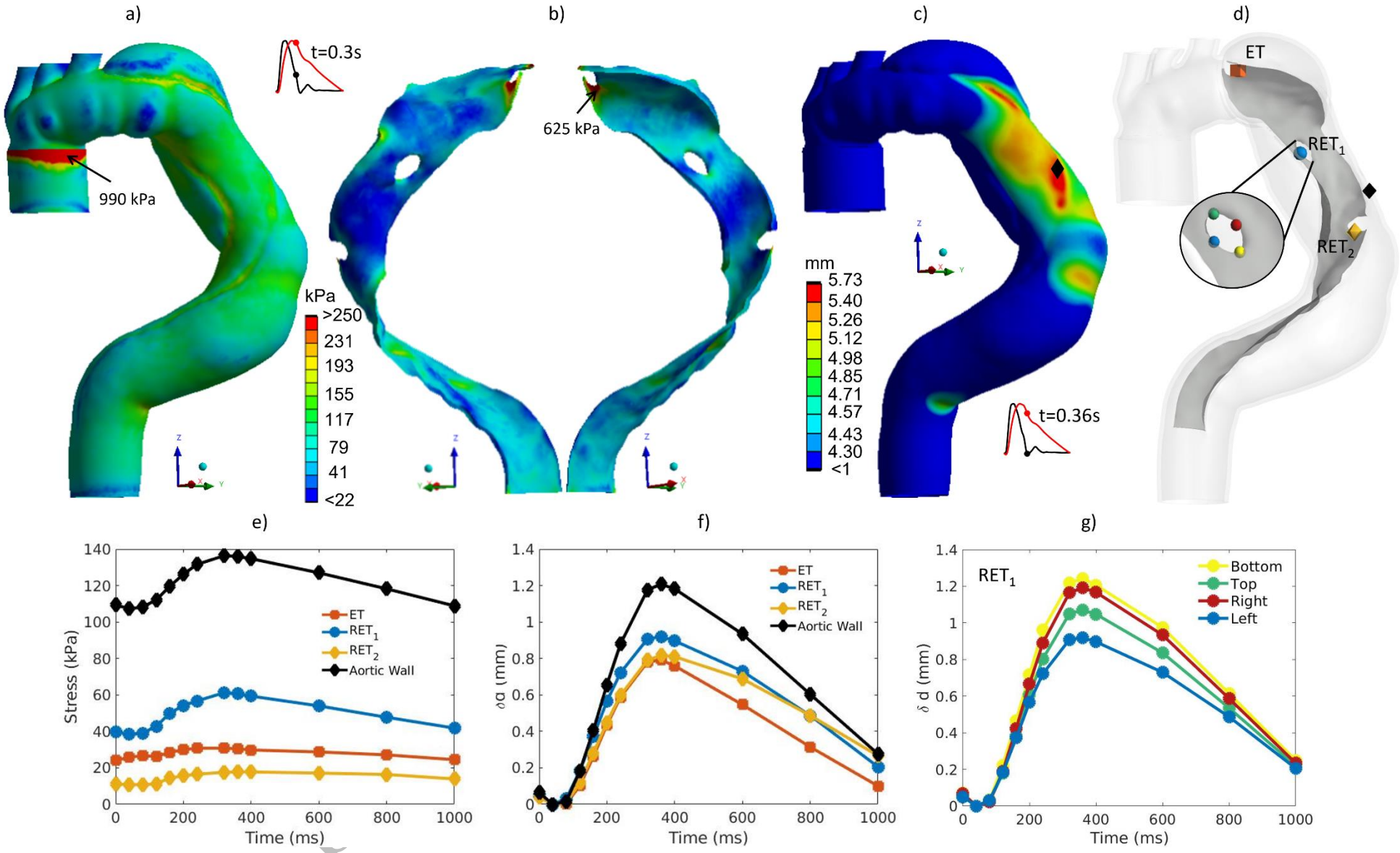

Figure 2 : Spatial distribution of von Mises stress for Full FSI at t=0.3s : a) at the aortic wall; b) at NIF -left: FL, -right : TL. c) Aortic wall spatial distribution of displacement magnitude for Full FSI at t=0.36s. d) Localization of points on ET (red cube), RET_1 (blue ball), RET_2 (gold diamond) and wall (black diamond); zoom of RET_1. Temporal evolution for Full FSI of e) stress, f) δd and g) δd at RET_1.

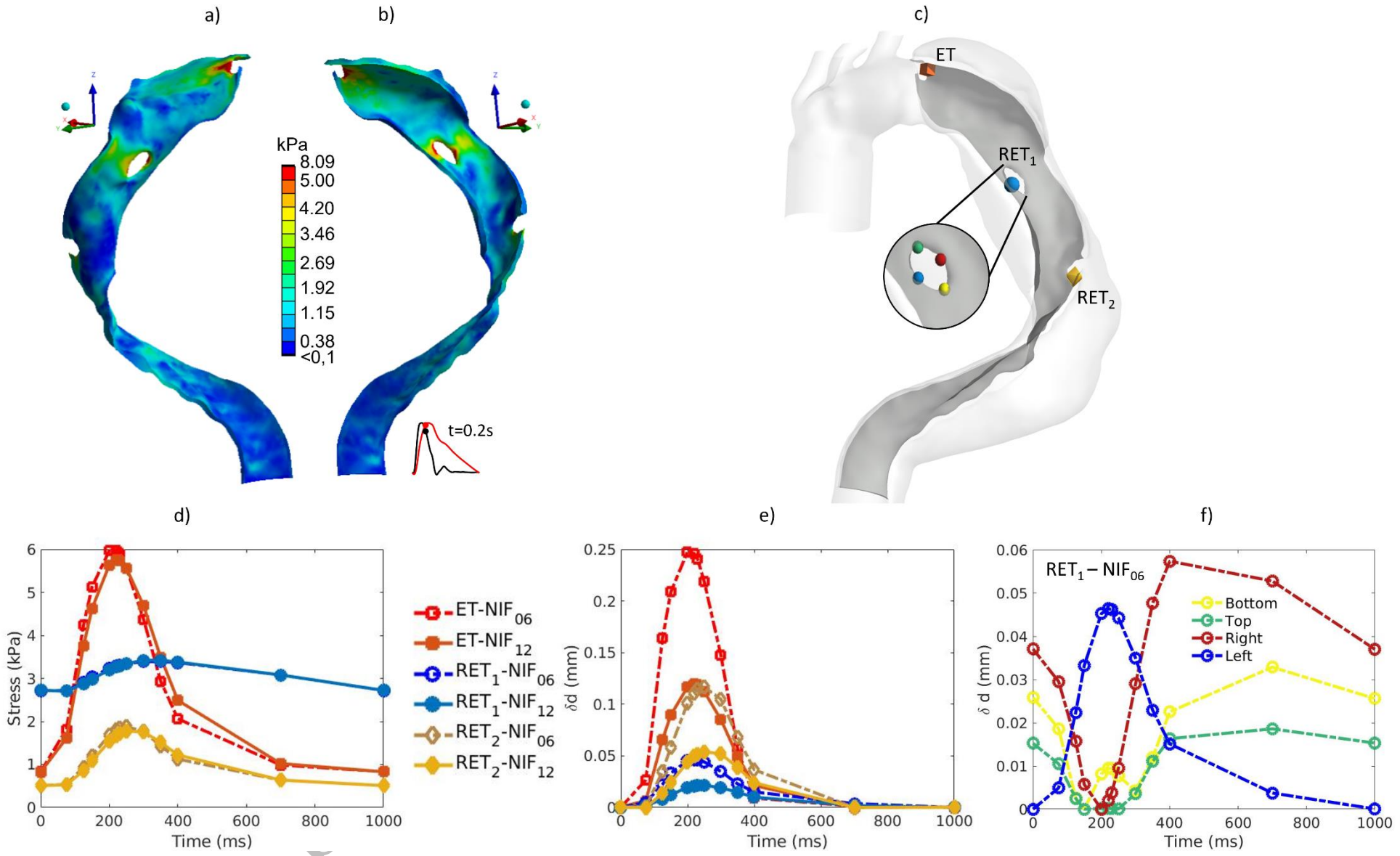

Figure 3 : Spatial distribution of von Mises stress for NIF FSI 12 a) FL view b) TL view. c) Localization of points on ET (red cube), RET_1 (blue ball), RET_2 (gold diamond) ; zoom at RET_1. Temporal evolution for NIF FSI of d) stress, e)δd, f)δd at RET_1-NIF_{06}

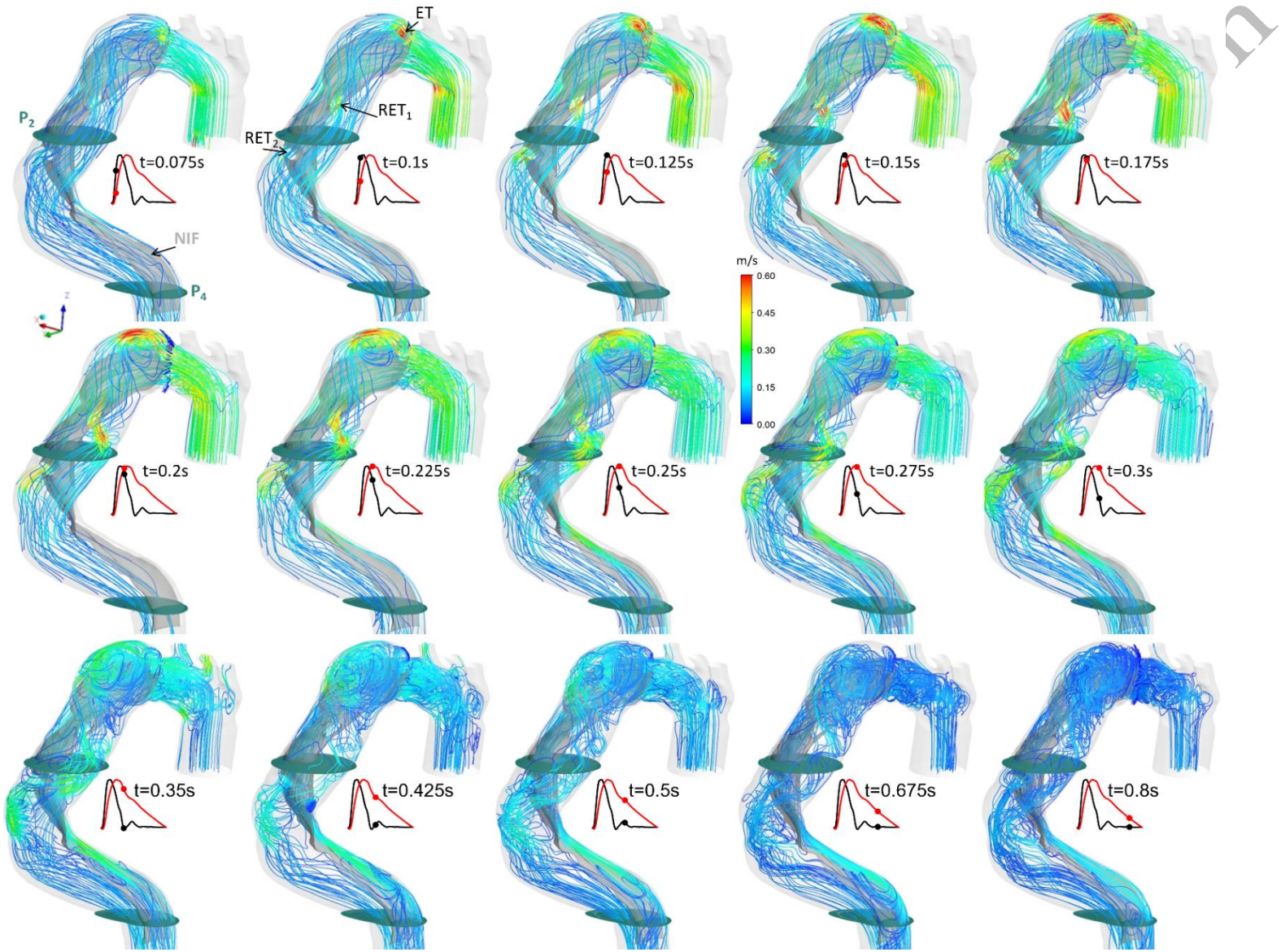

Figure 4 : Streamlines for Full FSI modeling plotted at different instants of the cardiac cycle. Colored by velocity magnitude

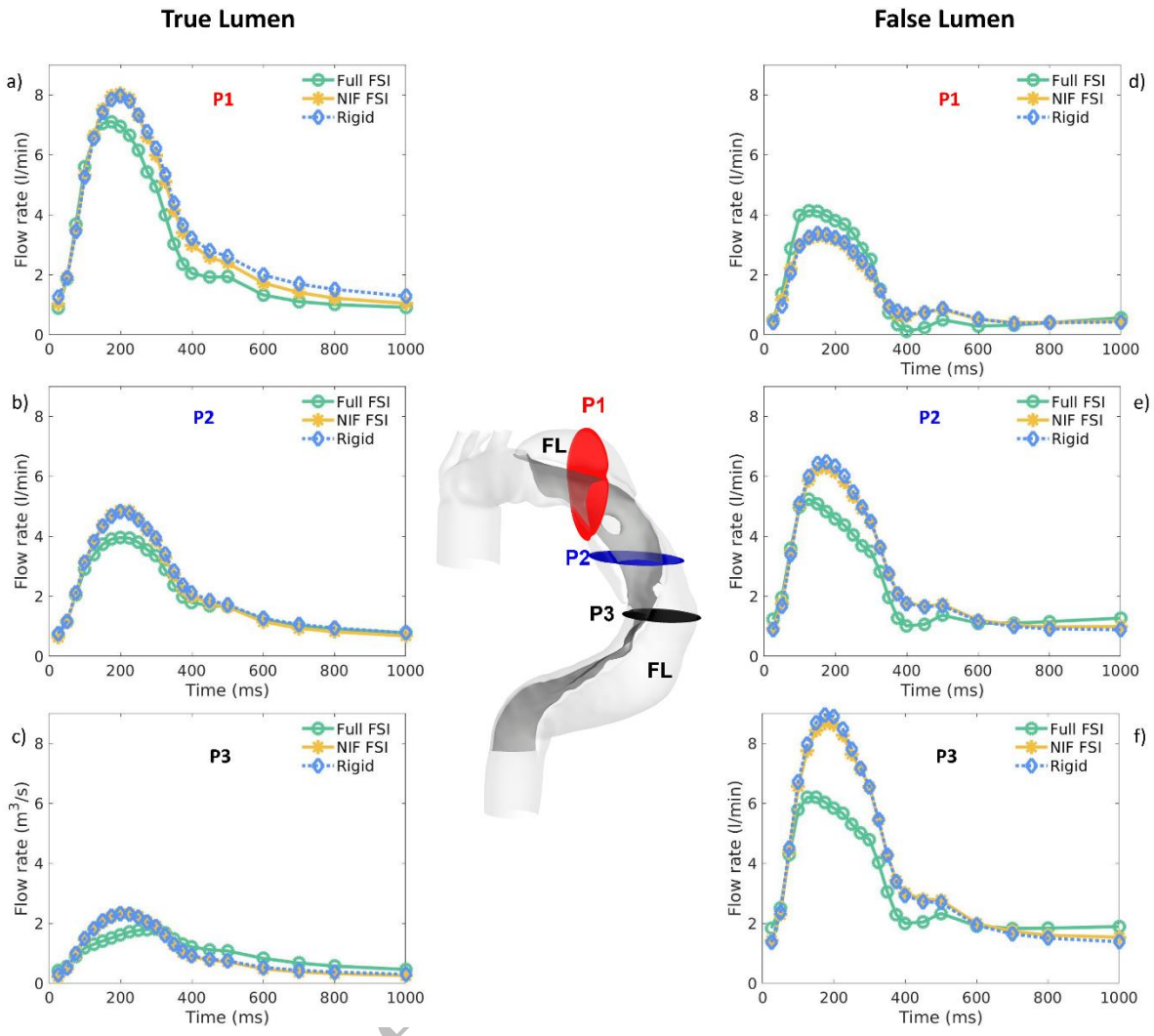

Figure 5 : Flow rate temporal evolution through TL (left column) and FL (right column) for P1 (a, d), P2 (b, e) and P3 (c, f) planes

pre proof

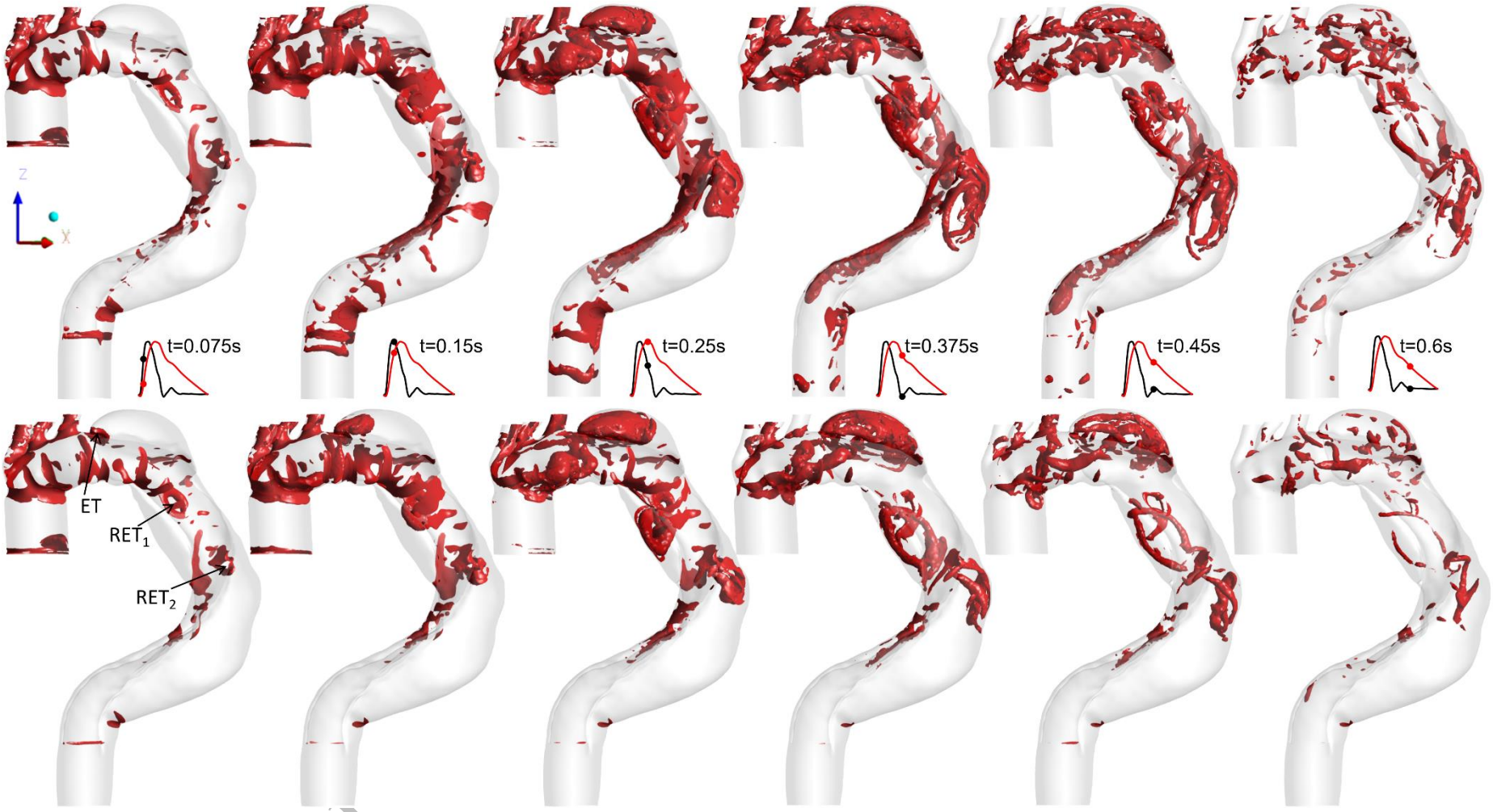

Figure 6 : Temporal evolution of λ_{ci} isocontours. λ_{ci} =19.5s^{-1}. First line : rigid wall modeling. Second line: Full FSI modeling.

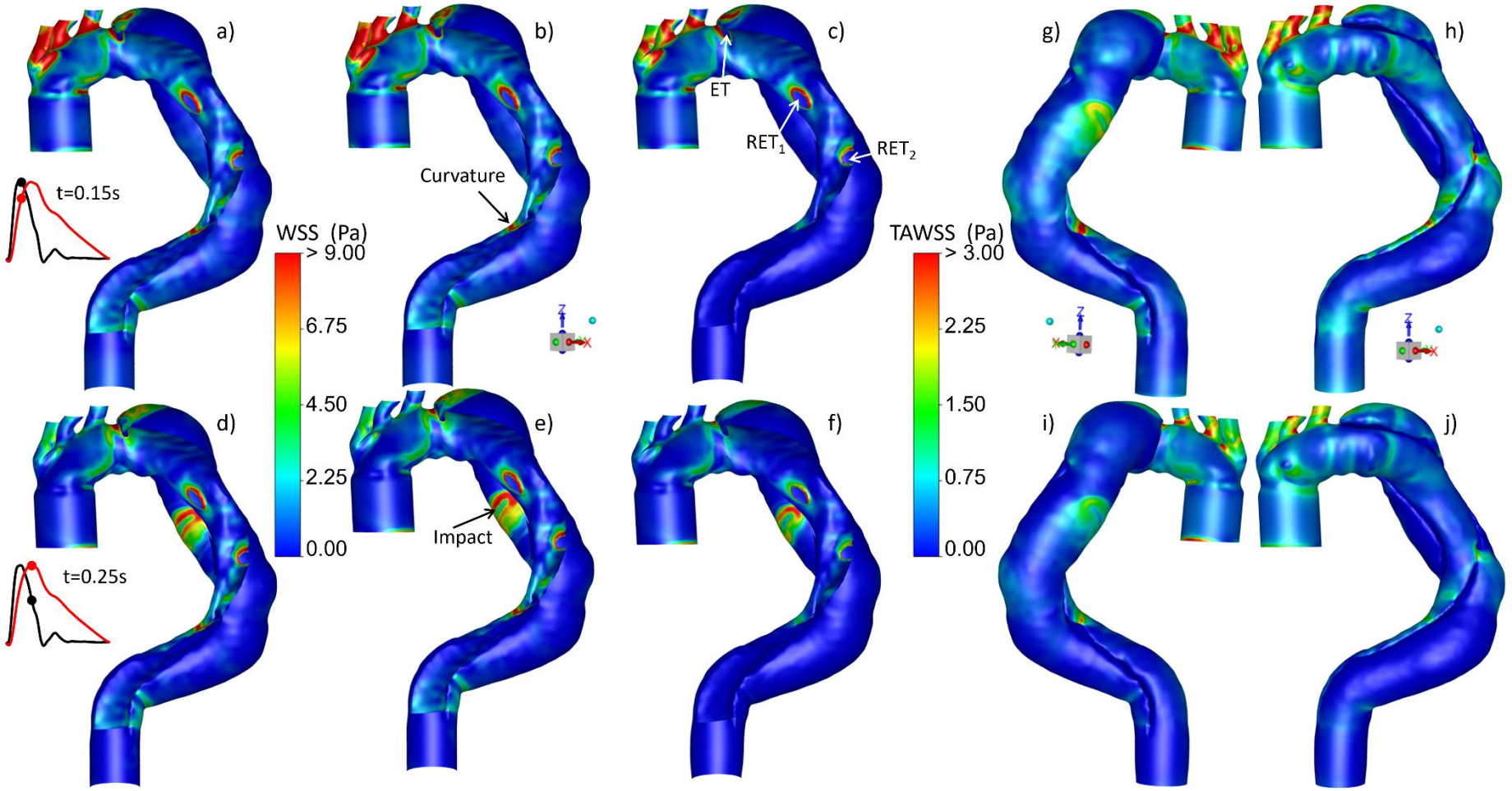

Figure 7 : WSS repartition with NIF in transparency for a and d) Rigid at t=0.15s and 0.25s respectively; b and e) NIF_{12} FSI at t=0.15s and 0.25s respectively and c) and f) Full FSI at t=0.15s and 0.25s respectively. TAWSS repartition for Rigid (g and h) and Full FSI (i and j).

pre

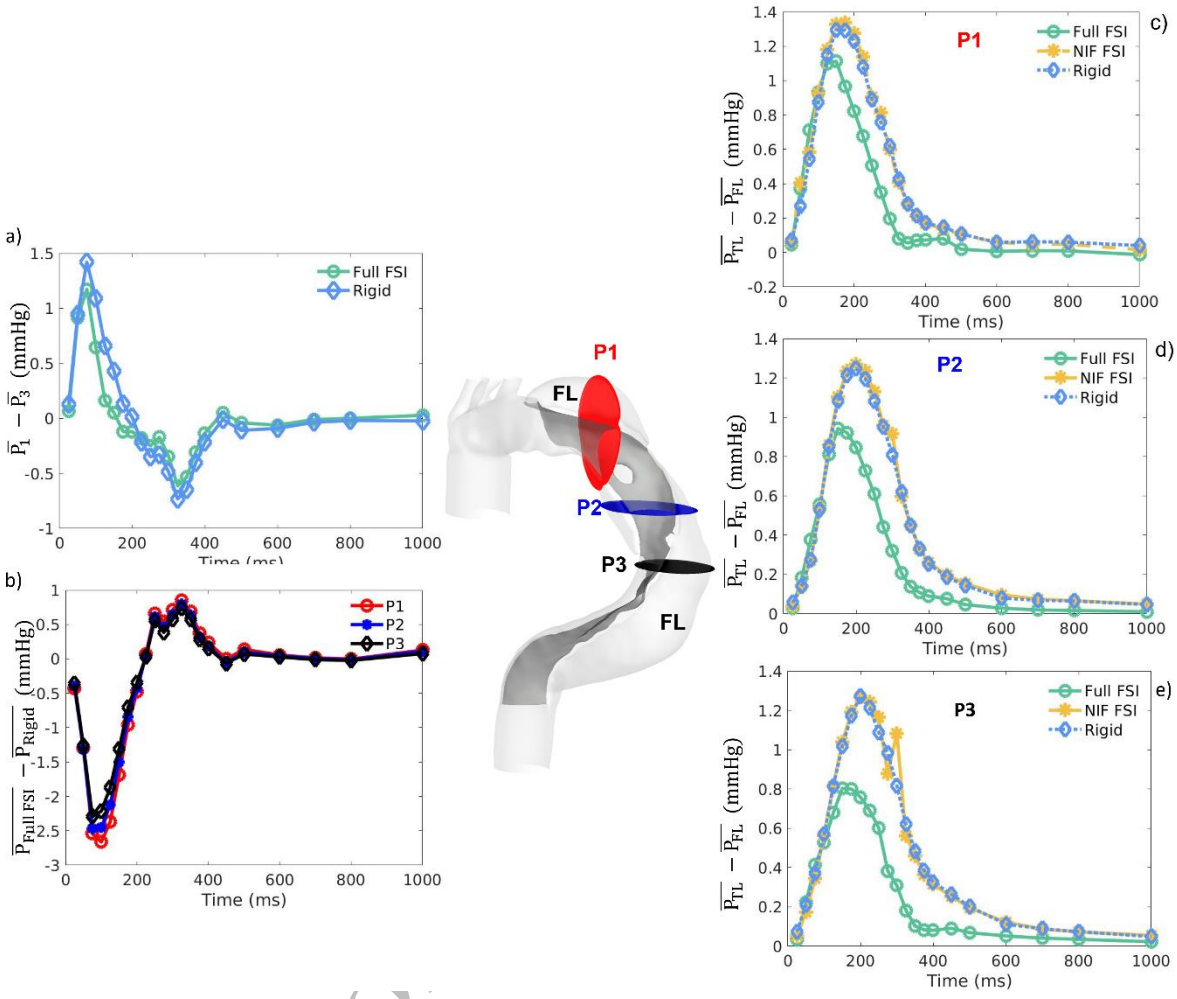

Figure 8 : a) Evolution of the difference of the mean pressure between P1 and P3 for Full FSI modeling and rigid one. b) Evolution of the difference of the mean pressure between Full FSI modeling and rigid one in P1, P2 and P3 planes. c) Evolution of the difference of the mean pressure between TL and FL for the 3 models in c) P1, d) P2 and e) P3 planes

pre proc